Revised: 26 January 2024 | Accepted: 16 May 2024

DOI: 10.1111/mice.13277

INDUSTRIAL APPLICATION

COMPUTER-AIDED CIVIL AND INFRASTRUCTURE ENGINEERING WILEY

Integrated urban land cover analysis using deep learning and post-classification correction

Lapone Techapinyawat[1] | **Aaliyah Timms**[1] | **Jim Lee**[2] | **Yuxia Huang**[3] | **Hua Zhang**[1]

[1]College of Engineering and Computer Science, Texas A&M University–Corpus Christi, Corpus Christi, Texas, USA

[2]College of Business, Texas A&M University–Corpus Christi, Corpus Christi, Texas, USA

[3]Conrad Blucher Institute, Texas A&M University–Corpus Christi, Corpus Christi, Texas, USA

Correspondence
Hua Zhang, College of Engineering and Computer Science, Texas A&M University–Corpus Christi, Corpus Christi, TX, USA.
Email: hua.zhang@tamucc.edu

Funding information
National Science Foundation, Grant/Award Numbers: 2050986, 2112631; National Aeronautics and Space Administration, Grant/Award Number: 80NSSC22K1670

Abstract

The quantification of urban impervious area has important implications for the design and management of urban water and environmental infrastructure systems. This study proposes a deep learning model to classify 15-cm aerial imagery of urban landscapes, coupled with a vector-oriented post-classification processing algorithm for automatically retrieving canopy-covered impervious surfaces. In a case study in Corpus Christi, TX, deep learning classification covered an area of approximately 312 km^2 (or 14.86 billion 0.15-m pixels), and the post-classification effort led to the retrieval of over 4 km^2 (or 0.18 billion pixels) of additional impervious area. The results also suggest the underestimation of urban impervious area by existing methods that cannot consider the canopy-covered impervious surfaces. By improving the identification and quantification of various impervious surfaces at the city scale, this study could directly benefit a variety of environmental and infrastructure management practices and enhance the reliability and accuracy of processed-based models for urban hydrology and water infrastructure.

1 | INTRODUCTION

Satellite imagery plays a key role in land cover studies (X. Li et al., 2019; Wulder et al., 2022; C. Zhang & Li, 2022). Landsat, a global observation program, offers consistent and extensive coverage over large areas, making it crucial for environmental monitoring and resource management (Amani et al., 2021; Roy et al., 2014; Shevyrev & Carranza, 2022). Similarly, due to its comprehensive coverage, the Sentinel program provides essential data that serve similar objectives (Bergsma & Almar, 2020; Scepanovic et al., 2021; T. Zhang et al., 2021). However, their limited spatial resolution is less effective in urban studies, where capturing the intricate details of urban landscapes is essential (D. He et al., 2022). This need for greater detail has led to a shift toward higher resolution imagery in the 1 to 4-m range, such as NAIP, IKONOS, and WorldView images (Goetz et al., 2003; J. Li & Bortolot, 2022; Zhu et al., 2022). Data of better resolutions are crucial for urban studies emphasizing accurate infrastructure network representation and disaster assessment (Braik & Koliou, 2024; Dunton & Gardoni, 2023; Kaur et al., 2023). The resulting high-resolution identification of impervious surfaces is essential for various urban water studies, such as hydrological modeling, flood risk assessment, and drainage infrastructure management (Du et al.,

2015; Ogden et al., 2011; Shust et al., 2005). It also plays a crucial role in the studies of urban infrastructure systems, particularly in estimating the potential of rooftop solar photovoltaic systems and supporting automated building damage assessments (Krapf et al., 2022; Q. Li et al., 2023; Nofal et al., 2024). Furthermore, accurate land cover classification is paramount in enhancing disaster resilience by providing critical input for models that predict the impacts of natural disasters (Kimpton et al., 2024). The requirement for high-resolution land cover data becomes evident as it highlights the effectiveness of these models, emphasizing their indispensable role in advancing the precision of urban studies and planning.

Recent advancements in aerial imaging technology have introduced remote sensing products with even higher resolutions at regional or national scales, for example, the 15-cm Hexagon aerial imagery (H x GN; Hexagon, 2021). This surpasses the capabilities of earlier datasets and offers broader coverage than small unmanned aircraft systems (UAS), which are limited in their survey extent. While using very high-resolution imagery in urban land cover studies is still rare, it has been increasingly available for many regions. This highlights a significant opportunity for improving urban land cover estimates, which could have substantial implications for urban planning and environmental monitoring at the city scale. The introduction of high-resolution aerial imagery suggests new research possibilities and the potential closure of a research gap in the efficient and accurate analysis of the big dataset—billions of pixels, compared to millions of pixels, in traditional images. However, the potential of using such sub-meter imagery for citywide land and infrastructure studies has not yet been fully explored.

A more fundamental research gap lies in analyzing the high-resolution imagery in urban land and infrastructure studies. Recognizing the complexity of urban landscapes presents a significant challenge for traditional classification methods. Methods such as random forest and support vector machine are foundational. However, they tend to produce data that may not fully capture the nuanced and varied nature of urban environments. Their inherent limitations become apparent in processing the rich textures and colors in high-resolution imagery (Khanwilkar et al., 2023; Y. Liu et al., 2013; Rana & Venkata Suryanarayana, 2020). As satellite and aerial imagery resolution improves, the demand for more advanced analytical techniques to process these data effectively increases. This need has propelled the emergence of deep learning (DL) as a promising field for urban land cover classification. DL's ability to analyze high-resolution imagery has been demonstrated through semantic segmentation models such as DeepLab, ResU-Net, and SegNet (Fu et al., 2021; Wang et al., 2021; Yoo et al., 2022). These models have shown notable success in classifying urban land cover with a level of detail previously unattainable, marking a significant advancement in the field.

Image-based approaches are adept at capturing small objects on the ground, yet they often fail to grasp the complexities of 3-D urban landscapes fully. Specifically, these methods struggle with accurately identifying features obscured by vertical elements such as tree canopies, which can conceal street pavements and roofs, often underrepresenting impervious surfaces. Such discrepancies can result in streets appearing narrower than their actual dimensions, artificially reducing the apparent street width and creating a bottleneck effect in land cover data (Figure 1a). Additionally, sidewalks aligned with these obscured areas may be depicted as disconnected, disrupting the continuity of the urban impervious surface network. This discontinuity impacts the quantitative accuracy of urban representation and poses significant challenges in calculating hydrological connectivity, which is crucial for accurately estimating surface runoff. Ensuring accurate representation of these connections is vital for urban hydrological studies, where the precise assessment of impervious surfaces informs effective stormwater management strategies (Sohn et al., 2020). Moreover, tree canopies can lead to overestimating vegetation areas by covering parts of roof features, highlighting the need for methodologies to accurately delineate urban features beneath canopy cover (Ning, Li, et al., 2022).

Despite advancements in urban feature classification, integrating auxiliary surface datasets has proven essential in enhancing the detection of features obscured by tree canopies. Technologies such as vehicle-mounted cameras provide street-level imagery capturing details often missed in aerial views (Ning, Ye, et al., 2022; Verma et al., 2021), while LiDAR technology delivers detailed point clouds that enhance the understanding of urban topography (Hu et al., 2021; L. Li et al., 2022; W. Zhang et al., 2021). However, these methodologies require the amalgamation of multiple independent processes, such as distinct analyses for street, sidewalk, and roof features, due to the limitations of using street imagery or altimetry LiDAR data for comprehensive feature corrections. For instance, the constraints imposed by the camera's perspective prevent street-level imagery from vehicle-mounted cameras from accurately correcting roof edges (Hou & Ai, 2020), and low point cloud density may not provide adequate detail for features beneath dense tree canopies (Hu et al., 2021). The reliance on extensive data collection and the need for varied datasets for different urban features extend the segmentation and labeling processes, complicating large-scale urban projects. Additionally, integrating data from diverse sources can challenge the consistency and accuracy of land cover classifications.

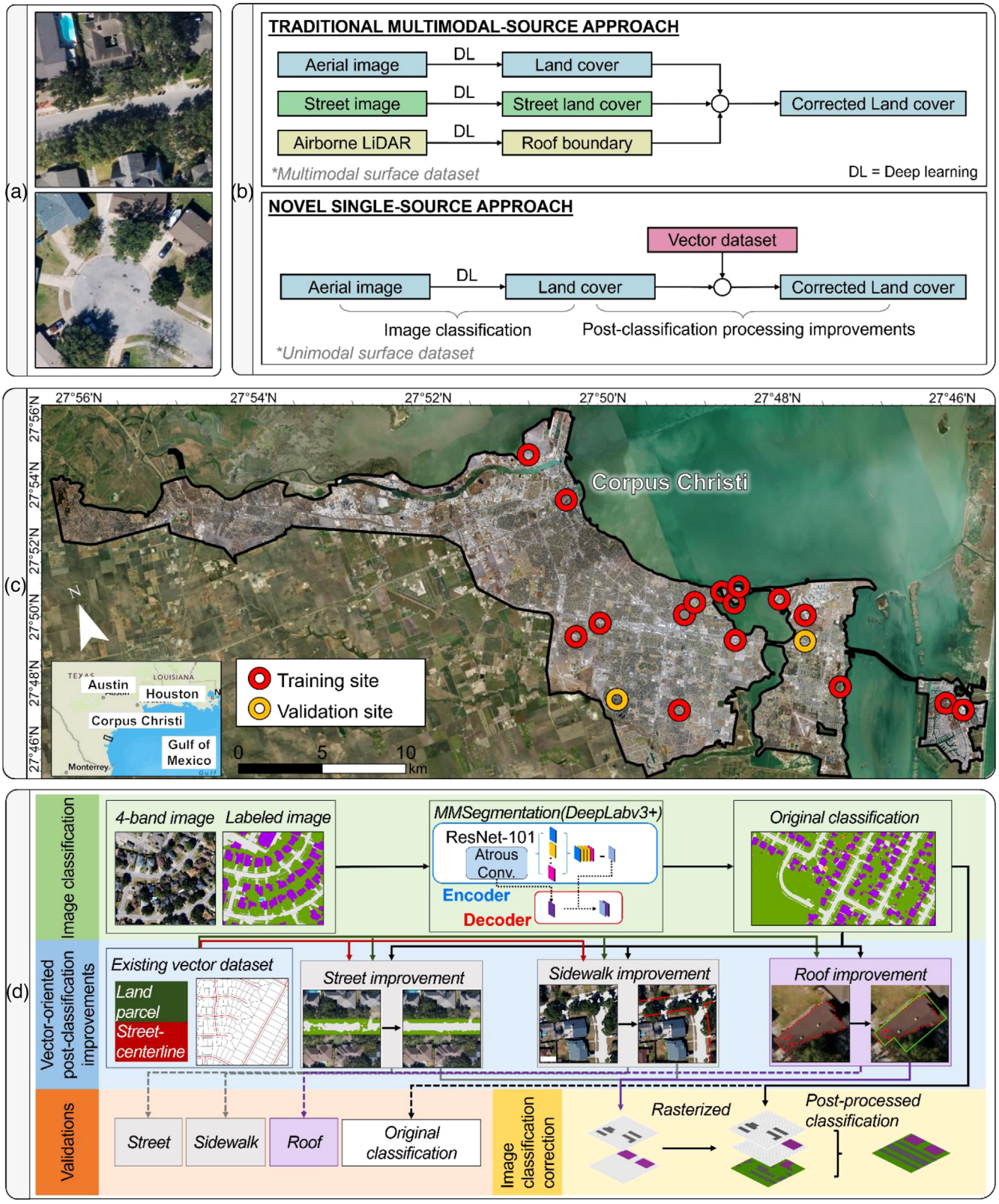

FIGURE 1 (a) Examples of the urban landscape with tree canopies; (b) existing methods versus novel approach (this study) for land cover feature correction under tree canopy; (c) study area. The black line indicates the coverage of HxGN images; (d) research framework.

In response to these challenges, this study introduces a novel method that integrates raster and vector analyses to improve the analysis of urban landscapes (Figure 1b). It is new in two aspects:

1. Innovative algorithms for urban feature analysis—Built on the topology of urban built features, the proposed roof and sidewalk algorithms are new, and the street algorithm is fundamentally different from existing approaches. These algorithms are enabled using state-of-the-art 15-cm aerial imagery at the city level that allows for unprecedented detail in urban feature analysis. In doing so, this method is able to correct various built features across complex urban landscapes at the billion-pixel level, contributing knowledge to engineering and geospatial big data analytics.
2. Unified raster-vector processing—This method is the first attempt to combine raster and vector domain processing for delineating urban impervious surfaces, in contrast to existing approaches that solely rely on raster datasets. Through a seamless transition from pixel classification to post-classification correction, it can maintain data integrity and consistency across various analysis stages and reduce dependency on additional surface datasets required in traditional methods.

Through a city-level case study, this study aims (1) to generate the most detailed city-scale land cover data possible, capturing small urban features across extensive cityscapes. These detailed data aid in urban hydrology studies by providing precise inputs for modeling water flow and flood risks, facilitating better water management. Additionally, it enables precise assessments of land use, urban planning, and infrastructure; and (2) to develop a vector-oriented post-classification improvement process that corrects misrepresentations of urban features obscured by tree canopies. This approach not only improves the accuracy of impervious surface identification, crucial for effective stormwater management, but also reduces the reliance on additional surface data collection. By combining the unprecedented detail of high-resolution aerial imagery with sophisticated vector-based correction processes, this study aims to achieve a more accurate and comprehensive understanding of urban landscapes. This enhanced understanding will leverage sights into existing infrastructure, facilitating improved urban planning and environmental management decision-making. Ultimately, this approach could lead to more sustainable and resilient urban development.

2 | MATERIALS AND METHODS

2.1 | Study area

The study area encompasses the city of Corpus Christi, TX, spanning an urban region of approximately 312 km^2 (Figure 1c). Zoning data reveal that this area predominantly consists of low-density and high-medium-density residential districts (City of Corpus Christi GIS Services, 2018). The median parcel block size measures 700 m^2. Situated on the Gulf of Mexico coast, the city has an average annual temperature of 22° C and an average yearly precipitation of 780 mm (National Centers for Environmental Information (NCEI), 2023). Dominant tree species in Corpus Christi vary in their canopy sizes, ranging from Sabal palms to live oaks (Poole et al., 2005; Qin et al., 2019). This poses challenges for effective land cover classification.

2.2 | Data

2.2.1 | Aerial imagery

The study employed 15 cm resolution aerial imagery from the Hexagon Content Program. This imagery has four spectral bands (red, green, blue, and near-infrared), enhancing its capability to discriminate between vegetative and non-vegetative surfaces. The images used in this study were acquired in 2021, covering an area of 312 km^2 with a total size of 50 GB.

2.2.2 | Vector data

The post-classification processing techniques for feature improvement beneath tree canopies used two vector datasets. The first dataset was a polyline shapefile of the centerlines of roads, streets, and alleys and included information on street width and connectivity (denoted by "street from" and "street to" fields). The information on connectivity facilitated the identification of cul-de-sacs. The second dataset was a polygon shapefile of the boundaries of land parcels. This dataset served a dual purpose: (1) delineating public right-of-way (comprising streets and sidewalks) for improvements in street and sidewalk features, and (2) distinguishing private property boundaries for improving roof features. The City of Corpus Christi provided both vector datasets (City of Corpus Christi GIS Services, 2023).

2.3 | Methods

The methods of this study included two primary phases (Figure 1d):

1. Generation of the most spatially detailed city-scale land cover data. The first phase involved image classification using an open-source DL method for pixel-level classification of 15-cm H×GN imagery. This phase surpasses the capabilities of conventional satellite and UAS imagery, providing highly detailed data for extensive cityscapes. It lays a solid foundation for the detailed representation of urban features and accurate subsequent analyses of feature corrections.
2. Development of a vector-oriented post-classification improvement process. Following the initial classification from Phase 1, the second phase involved post-classification improvements based on a new vector-oriented approach. This phase detects and quantifies impervious surfaces hidden by tree canopies using statistical and GIS analyses integrated with public urban infrastructure data. This approach minimizes reliance on auxiliary surface datasets and enhances the correction accuracy at the feature level.

This study was built on a set of four assumptions, reflecting the characteristics observed within our study area, and is based on the topology of roofs and streets (Dunton & Gardoni, 2023). Assumptions include: (1) sidewalk alignment runs parallel to streets; (2) sidewalk presence is considered either entirely present or absent along corresponding street segments; (3) sidewalk width is consistent and in compliance with the city's established engineering codes (Order of the City Council, 2004); (4) residential roof geometry features orthogonal designs. Each phase included validation, addressing classification accuracy at the pixel level, and correction accuracy at the feature level.

2.3.1 | Image classification using deep learning

The land cover was categorized into five classes: (1) paved surface class, including various asphalt and concrete pavements of streets, sidewalks, driveways, uncovered patios, runways, and bridges; (2) building, including residential properties, commercial properties, industrial properties, containers, towers, and mobile homes; (3) vegetation, including trees, grass, and shrubs; (4) non-vegetation, accounting for bare soil, beaches, and ripraps; and (5) water, consisting rivers, lakes, bays, ponds, and swimming pools. A two-level hierarchical classification scheme was adopted to reflect the main features observed in urban areas. The first level distinguished between built-structure impervious areas, non-built structure pervious areas, and water surfaces. A further distinction was made between paved surfaces and buildings in the built-structure impervious category based on their geometric and color characteristics. Pervious areas were subdivided into vegetation and non-vegetation, based on their distinct responses to near-infrared and red image bands. This structured approach could benefit the deep learning model by helping it learn and differentiate between these distinguished patterns.

A comprehensive set of training samples was systematically established to reflect the diverse land cover characteristics of the study area. A total of 16 training locations were chosen, each covering 40,000 m^2 (Figure 1c). Among these sites, four were labeled for representing residential areas, two for commercial zones with low-rise buildings, one for downtown areas with high-rise buildings, two for highways and airport runways, and seven for areas of undisturbed land. After labeling, each site underwent an augmentation procedure involving rotation to ensure the model's robustness against variations in orientation, including the diverse orientations of urban layouts. In detail, each site was segmented into smaller 112.5 × 112.5 m image chips and subjected to a data augmentation procedure involving rotations at 0°, 120°, and 240°, incorporating vertical and horizontal strides of 11.25 m that accounts for 10% of the image dimension (Figure 2). This led to a total of 1591 labeled samples from the 16 training sites.

The MMSegmentation toolbox was employed to perform detailed pixel classification, manipulating aerial imagery with a resolution of 15 cm (MMSegmentation Contributors, 2020). The specified model, "DeepLabV3+," was configured with model weights set to false and utilized a ResNet-101 backbone (Chen et al., 2018; K. He et al., 2016). This backbone incorporates atrous convolution, enabling the model to capture multi-scale information. The training process was developed with a maximum of 60 epochs and an early stopping mechanism to halt training if no further model improvements were observed. This mechanism used validation loss as an indicator for improvement. Training was terminated if the validation loss did not decrease significantly. Default early stopping parameters were set to a delta of 0.01 and a patience of 5. Experimenting with higher epoch numbers could yield improved results; however, it is essential to consider the trade-off between potential improvement and increased training time. The model employed a dynamic learning rate, initially set within the range of 6.92×10^{-5} to 6.92×10^{-4}, and then adjusted adaptively based on the model's performance during training.

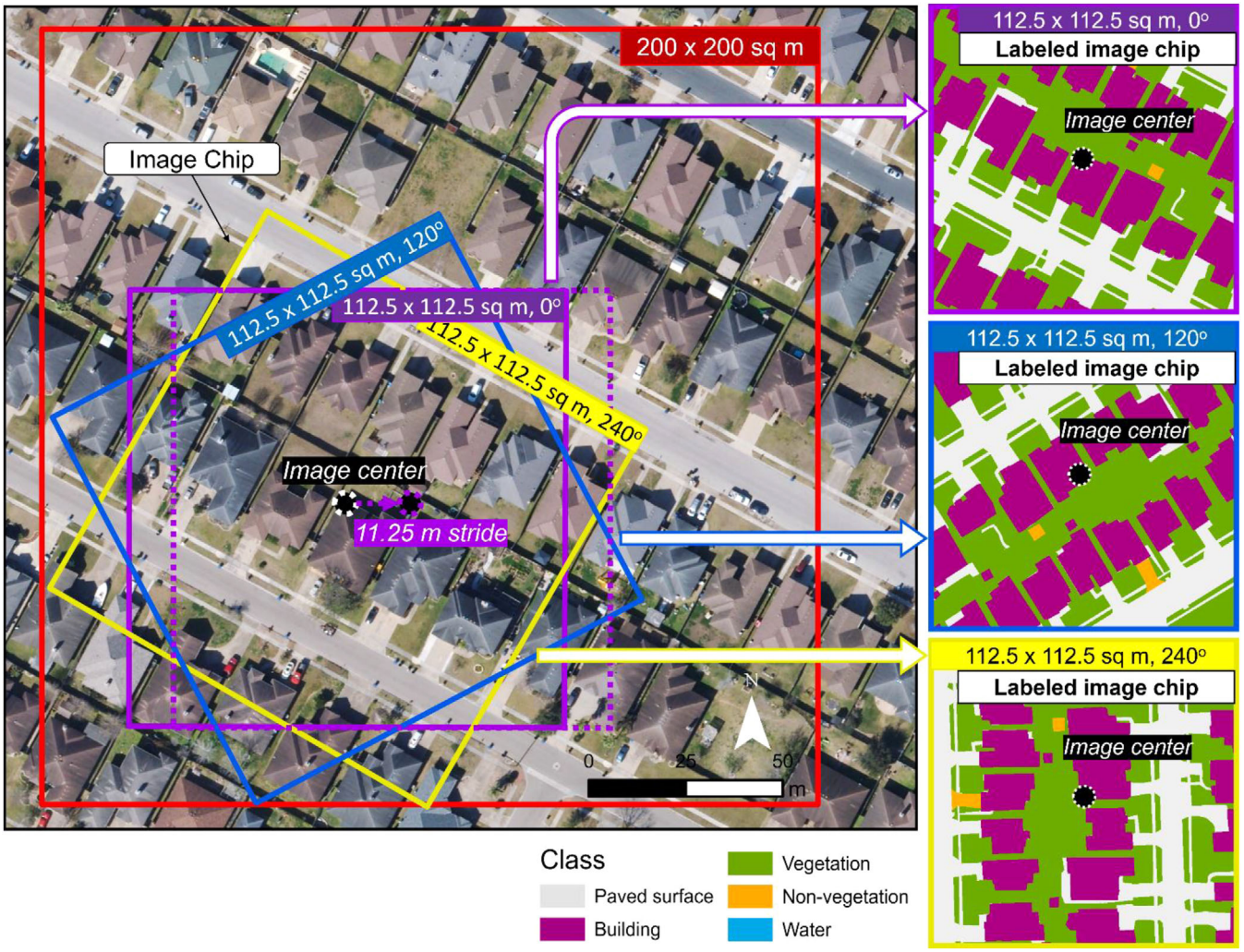

FIGURE 2 Image chips with orientation-based augmentation, labeled by class. The method involves generating labeled image chips, rotating (0°, 120°, 240°). Then, reposition it using an 11.25 m stride to apply the process at subsequent locations.

2.3.2 | Vector-oriented post-classification improvements

The DL-derived original classification result was converted from a raster to polygons. Street centerlines and land parcel boundaries (see Section 2.2.2) were integrated into the landcover polygons using the same spatial reference. The post-classification processing phase focused on enhancing classifications beneath tree canopies for three built features: (1) streets, (2) sidewalks (including parallel and cul-de-sac), and (3) building roofs.

Street improvement

Street improvement efforts focused on correcting misclassified areas where tree cover was inaccurately identified in place of streets. This was achieved using the vector data of street centerlines with an embedded attribute indicating street width (bold red line in Figure 3a). It was essential to ensure the continuity of these street centerlines. The analysis required dissolving broken centerlines into continuous segments at each change in direction and dividing extensive centerlines at intersections. In the case of abrupt irregularities along the adjusted centerline, an optional smoothing algorithm was applied to mitigate and enhance the smoothness of the centerline. A Polynomial Approximation with Exponential Kernel algorithm with a tolerance setting of 10 m was utilized in this case (Bodansky et al., 2002). Then, the centerline was buffered on both sides by half the street width based on the city's data. The resulting buffer polygons were created to delineate the dimensions of streets (Figure 3b). Finally, the buffer polygons were merged at intersections to create a continuous street polygon (Figure 3c).

Sidewalk improvement

Street improvement was followed by sidewalk improvement. To improve the computational efficiency, the polygons of classification results were clipped to the extent

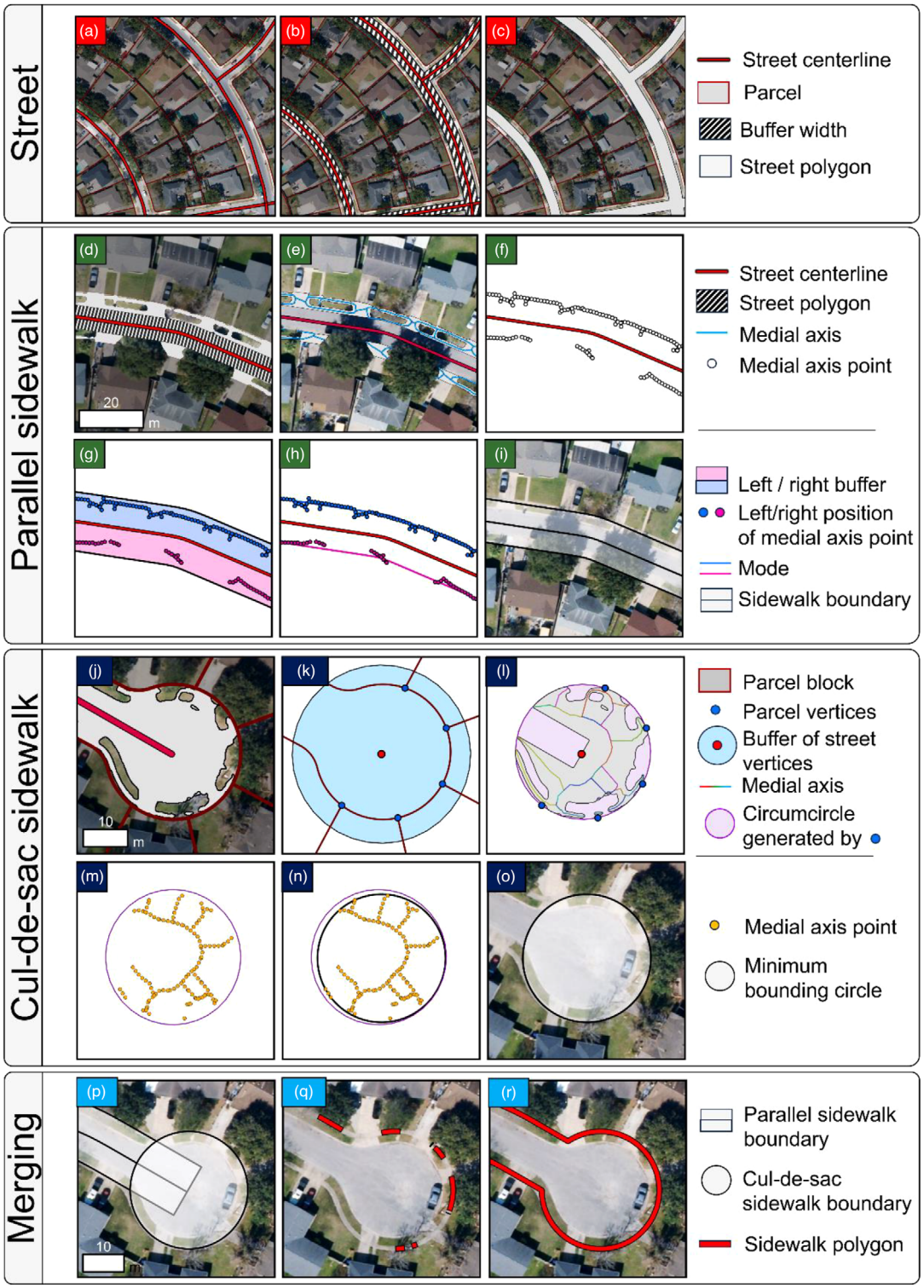

FIGURE 3 The procedures of street and sidewalk improvements: (a) street centerline located in a public right-of-way; (b) generate a buffer on both sides of the centerline with the street width field; (c) result of a street polygon; (d–i) parallel sidewalk improvement; (j–o) cul-de-sac sidewalk improvement; (p–r) merging parallel and cul-de-sac sidewalks.

of public rights of way because sidewalks were exclusively within the public right of way. The clipped polygons were dominated by paved surfaces (such as asphalt and concrete) and vegetation (including trees and sidewalk gardens), while water and non-vegetation classes were negligible. Notably, the clipped polygons were not expected to include any buildings. If building classifications were encountered in this region, these building classifications were reclassified as part of the paved surface class. This led to the confined paved surface class within the public right of way (Figure 3d).

To appropriately represent the sidewalks, any paved surface polygons within the public right of way needed to be removed where they overlapped with street polygons (Section 2.3.2—Sidewalk Improvement). The resulting paved polygons included sidewalks, such as parallel or cul-de-sac variants.

For parallel sidewalks, the improvement included four steps. First, the polygons of the paved surface derived from the image classification were used to generate a medial axis, an estimate of the sidewalk centerline (Figure 3e). Even though tree canopies might partially cover some sidewalks, the positions of those sidewalks were still inferred by determining the distance between their visible medial axes and the associated street centerline. Second, sample points were generated along the medial axis at 1-m intervals to represent the sidewalk center. The sample points close to street polygons (e.g., within 20 cm) were removed, as they might represent curbs and gutters (Figure 3f). Medial points were separated for left and right-side analyses, and two buffer polygons were created for each side (Figure 3g). Third, mode calculations were conducted to predict the distance of sidewalks from the street. The distances from each point to the street centerline were calculated and labeled with respective distances and street identifiers, then rounded to the nearest 0.5 m increments (Equation 1). These rounded distances formed the set M, consisting of distances $D_{(i,\ rounded)}$ for each point across a street segment, with i ranging from 1 to n, where n is the count of points measured on that particular side. Each distance in the set contributes a "1" if it matches the distance x or "0" if not. The mode of these distances, $Mode_{distance}$, identifies the most frequent distance from the centerline on either the left or right side.

$$Mode_{distance} = \max_{x \in M} \sum_{i=1}^{n} \begin{cases} 1 & if \quad x = D_{i,rounded} \\ 0 & if \quad x \neq D_{i,rounded} \end{cases} \tag{1}$$

To determine the presence of sidewalks, the analysis applied a threshold for medial axis points per street segment length. This threshold, set at 15%, meant that no sidewalk was generated if the paved surface along a 100-m street segment was less than 15 m. This aimed to avoid mistaking driveways for sidewalks. Fourth, buffer zones were created from street centerlines on both sides based on the calculated modes of street-sidewalk distance (Figure 3h,i). These polygonal boundaries indicated the positions of the parallel sidewalks.

For cul-de-sac sidewalks, the process began with utilizing the previously created paved surface class polygon, street centerline, and land parcel (Figure 3j). The procedure included five steps. First, the polygon of the paved surface was clipped within the cul-de-sac areas, leading to the intersecting points between the polygons of parcel block vertices and the polygons of the public right-of-way (shown as blue dots in Figure 3k) to help form these circles. Second, dead-end street segments were identified using street connectivity, followed by circular buffers around their vertices, focusing on retaining only those at the dead ends. Third, based on those vertices, a circle was generated that solely enclosed the public right-of-way and cul-de-sac area. Different vertex selections could yield different circles. R_{ijk} is the radius of a circle defined by three vertices (P_i, P_j, and P_k) from the set. Among all circles defined by the available vertices, the optimal circle is the one with the smallest radius, and the associated vertices are denoted as P_a, P_b, and P_c (Equation 2). If there are only three vertices, the only circle is considered optimal. Non-circular cul-de-sacs were detected using spatial analysis to check if the generated circles overlap surrounding land parcels. The detected non-circular cul-de-sacs were excluded from further analysis.

$$(P_a, P_b, P_c) = \min_{(P_i,P_j,P_k)} R_{ijk}, \text{ if } n \geq 3 \tag{2}$$

Fourth, this optimal circle was selected to establish the medial axis (Figure 3l). Where the medial axis lines might represent driveways or extensions of parallel sidewalks, trimming of these lines using the parcel boundaries occurred. Fifth, the remaining segments were converted into medial points (Figure 3m). Finally, the minimum bounding circle was created for the targeted cul-de-sac sidewalk (Figure 3n,o).

Next, the established polygons of parallel and cul-de-sac sidewalks were merged into a continuous network through three steps. The first step was removing overlapping areas at transition zones and street intersections (Figure 3p). The outer boundaries were converted into a network of sidewalk centerlines. Centerlines intersecting with the vegetation class were clipped for areas under trees. Next, buffers aligned with observed or city-standard sidewalk widths were applied. The post-classification processed sidewalks are depicted in Figure 3q. Intersections with the vegetation class were not clipped for a continuous network as shown in Figure 3r.

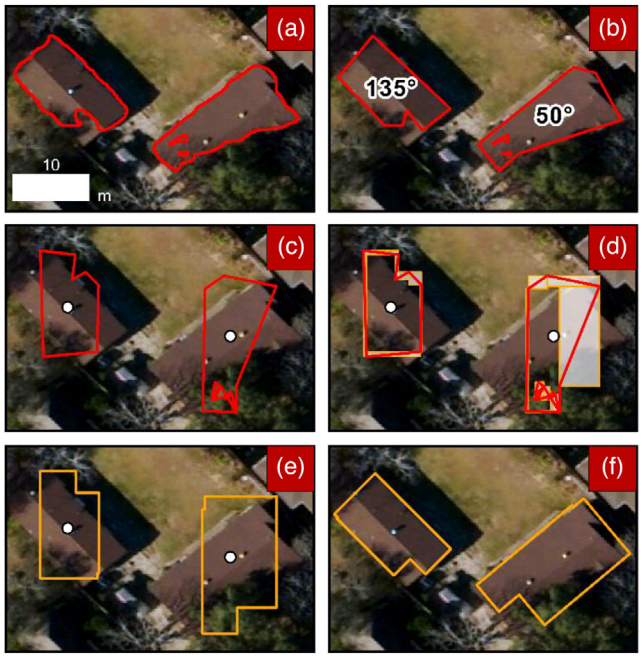

FIGURE 4 The procedures of roof improvement: (a) original roof outlines; (b) simplified roof outlines and their major orientations; (c) rotated roof outlines to the X and Y axes; (d) minimum bounding box of lines of roofs; (e) outer boundary of dissolved bounding boxes; (f) result of improvement.

Roof improvement

The principle of roof improvement relies on the inherent orthogonal shape of roofs, irrespective of their orientation. When an edge of a roof polygon derived from the image classification is neither parallel nor perpendicular to its orientation, the roof might be partially covered by tree canopies. The gap between the assumed orthogonal shape and the original roof shape indicates the need for correction.

An axis-aligned minimum bounding box algorithm was employed to identify the minimum orthogonal bounding boundary for each building. This algorithm is based on fixed X (West-East) and Y (North-South) axes, so a four-step rotation procedure was applied.

First, roof polygons within parcel boundaries were extracted from the classification results (Figure 4a). The selected polygons were simplified to highlight their primary outlines by filtering out north-south and east-west boundaries, a gridded raster classification conversion characteristic. This was conducted using the Douglas–Peucker method with tolerance levels ranging between centimeters and meters (Douglas & Peucker, 2011). While a lower tolerance might capture only parts of roofs under tree canopies, a higher one might over-simplify and misrepresent the roof structures. The analysis began with a 50-cm tolerance and was iteratively adjusted by 50-cm increments. The final tolerance level selected was the one that best preserved essential roof details.

Second, the simplified polygons were transformed into line segments. Each roof polygon splits at every vertex to create smaller roof segments. The orientations of these segments were adjusted from 0 to 360 degrees to 0 to 180 degrees; for example, east-west and west-east orientations were described as 90 degrees. This approach simplified analysis by focusing on segment orientation, not direction. The adjusted orientation for each segment Θ'_j was defined by Equation (3). The primary orientation, Θ_{major}, was determined by the cumulative length of segments S_j sharing similar orientations, iterating from $j = 1$ to m, where m represented the total number of segments, as stated in Equation (4). The result was recorded as the predominant orientation for each roof (Figure 4b).

$$\Theta'_j = \left(\arctan\left(\frac{y_{j2} - y_{j1}}{x_{j2} - x_{j1}}\right) \times \left(\frac{180}{\pi}\right)\right) \bmod 180 \quad (3)$$

$$\Theta_{major} = \max_{\Theta'}\left(\sum_{j=1}^{m} S_j \times \begin{cases} 1 & \text{if } \Theta'_j \approx \Theta' \\ 0 & \text{if } \Theta'_j \not\approx \Theta' \end{cases}\right) \quad (4)$$

Third, the roof polygons were rotated around their centroids (c_x,c_y) based on their predominant orientations to align with the north-south or east-west axes (Figure 4c). For each vertex (x_i,y_i), iterating from $i = 1$ to n (where n represented the total number of vertices in the polygon), the vertices were rotated to align with Θ_{major}. (x_i',y_i') were the rotated coordinates for each vertex i (Equation 5).

$$\begin{aligned}\{(x'_i, y'_i)\}_{i=1}^{n} = \{&((x_i - c_x)\cdot\cos(-\Theta_{major}) \\ &-(y_i - c_y)\cdot\sin(-\Theta_{major}) + c_x, \\ &(x_i - c_x)\cdot\sin(-\Theta_{major}) \\ &+(y_i - c_y)\cdot\cos(-\Theta_{major}) + c_y)\}_{i=1}^{n}\end{aligned} \quad (5)$$

Fourth, the rotated roof polygons were split into line segments at their vertices. An orthogonal bounding box was generated for each line segment (Figure 4d). Any lines that deviated from the north-south or east-west orientation would suggest the interference of tree canopy. A slight buffer was added to these bounding boxes to ensure their continuity. Each roof's bounding boxes were merged to generate a new roof polygon (Figure 4e). For the final step, as depicted in Figure 4f, the roof polygons were rotated back to their original orientations using Equation (6). Here, (x_i'',y_i'') were the coordinates of vertex i after being rotated back, indicating the final positions of each vertex after adjustments to align with the roof's predominant orientation.

$$\{(x_i'', y_i'')\}_{i=1}^{n} = \{((x_i' - c_x) \cdot \cos(\Theta_{major}) - (y_i' - c_y) \cdot \sin(\Theta_{major}) + c_x, (x_i' - c_x) \cdot \sin(\Theta_{major}) + (y_i' - c_y) \cdot \cos(\Theta_{major}) + c_y)\}_{i=1}^{n} \quad (6)$$

2.3.3 | Updating image classification

After obtaining feature correction polygons for streets, sidewalks, and roofs, the next step was to update the original classification accordingly. The original classification was in raster format, so the vector corrections were converted to rasters. This conversion demanded alignment as depicted in Figure 5a. The process designated the retrieved streets and sidewalks as the paved surface class and the roofs as the building class. Both cell size and reference coordinates were aligned with the original raster. When combining these corrected rasters with the original classification, the system assigned the lowest priority to the original classification during the union, indicating that discrepancies were resolved in favor of the corrected data. This approach directly impacted the classification result by including additional impervious areas beneath tree canopies, previously undetected in the original data. The updating process improved the representation of impervious areas and enhanced the accuracy and connectivity of ground features in urban landscapes.

2.3.4 | Validation

Validation of image classification

The land cover classification was validated against ground truth data generated through the on-screen digitalization of H×GN imagery. This process involved two validation sites, each encompassing 160,000 m^2. These sites were distinct from the areas used for training the DL model, ensuring an unbiased assessment of the model's performance. Google Maps and Google Street View were utilized as additional resources to aid in the differentiation of bare soils from concrete pavements. For a thorough evaluation, 10 million random points were selected across the validation sites and compared against the raster output of the DL-based image classification.

A confusion matrix assessed the agreement between the classified results and the ground truth. The kappa statistic, quantifying agreement beyond what is expected by chance, was calculated using Equation (7). Here, x_{ii} represents the number of instances correctly predicted for each class i. The total number of observations is denoted by N, and k is the number of classes determined from the confusion matrix. The terms row_i and col_i in the equation correspond to the sum of the observations in the ith row (total actual instances of class i) and the sum of the observations in the ith column (total predicted instances of class i), respectively. This kappa value, with a result close to 1, indicates a near-perfect level of agreement between the classified and actual data.

$$\kappa = \frac{\sum_{i=1}^{k} x_{ii} - \frac{1}{N}\sum_{i=1}^{k} (\text{row}_i \times \text{col}_i)}{N - \frac{1}{N}\sum_{i=1}^{k} (\text{row}_i \times \text{col}_i)} \quad (7)$$

Validation of feature correction

Each feature possesses distinct characteristics such as area, length, and shape, necessitating varied validation approaches. The results of street, sidewalk, and roof improvements were evaluated separately. The ground truth data were digitized using 15-cm resolution 4-band aerial images, supplemented with high-resolution Google satellite maps and Google Street View for all these validations. Additionally, LiDAR point cloud data were used for roof validation.

Street validation involved comparing the classified street areas with the ground truth. For this analysis, 50 streets were randomly selected throughout the study area. The ground truth was established by measuring the areas of visible streets on aerial imagery, including those sections obscured by tree canopies. Street features were validated by comparing the areas from the original DL classification ("before") and the post-classification processing improvement ("after") to the ground truth. The validation process focused on ensuring the classified street areas corresponded accurately to the actual streets. Key evaluation metrics included mean absolute error (MAE), mean absolute percentage error (MAPE), and R-squared (R^2), alongside completeness, aiming for 100% to demonstrate that the algorithm has successfully identified and reconstructed all street areas under tree canopies. Furthermore, the Wilcoxon signed-rank test was utilized to assess statistical significance in the differences between the "before" and "after" classifications (Wilcoxon, 1992).

Sidewalk validation involved comparing the generated lines and the ground truth concerning length. For this study, 100 street segments were randomly selected across the entire study area. Each segment could include sidewalks on both sides, a cul-de-sac, or neither. The ground truth was established by measuring the lengths of visible sidewalks on aerial imagery, including those sections obscured by tree canopies. The sidewalk features were validated by comparing the lengths of the original DL classification ("before") and the post-classification processing improvement ("after") to the ground truth. To be considered valid, sidewalk lines must overlap accurately with the actual sidewalks. Validation metrics included MAE,

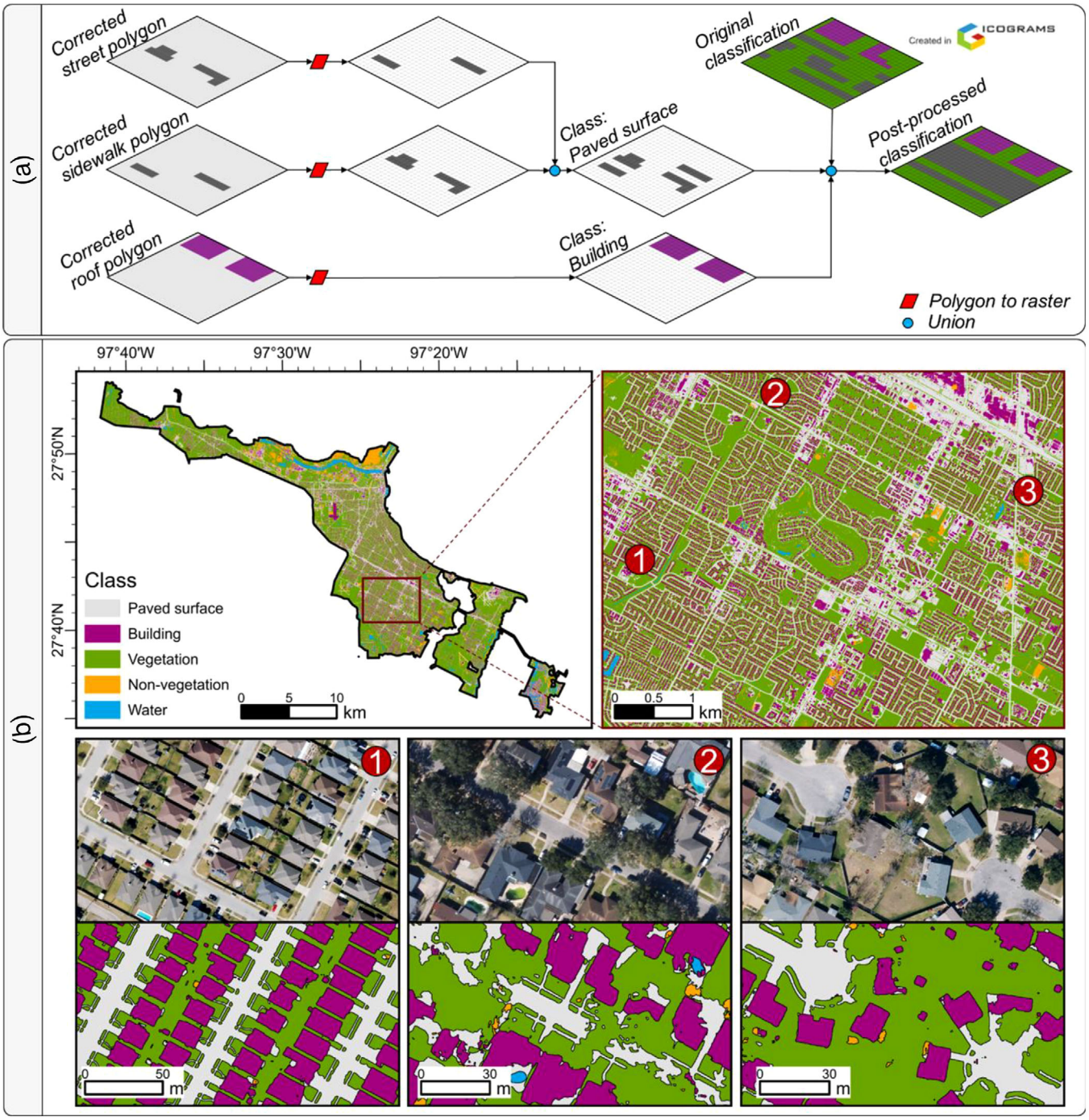

FIGURE 5 (a) Image classification updating procedure; (b) the results of image classification at three example locations.

MAPE, and R^2, alongside completeness, which ideally reaches 100% to indicate that the algorithm has successfully delineated and connected all sidewalk gaps under tree canopies. Furthermore, the Wilcoxon signed-rank test was applied to assess statistical significance in the differences between the "before" and "after" sidewalk features, underlining the effectiveness of the improvement.

Roof validation involved comparing the generated building class area within parcel blocks and the ground truth. Roof validation focused on the building class. A sample of 200 random parcel blocks of varying sizes was analyzed. Within each block, the area of the building class from both the original and post-classification improvement was compared against the ground truth. Moreover, roofs were categorized into four distinct groups based on their design and interaction with tree canopies: simple roofs not covered by vegetation (SN), complex roofs not covered by vegetation (CN), simple roofs covered by vegetation (SV),

TABLE 1 Confusion matrix of the image classification results.

		Predicted class						
	Class value	**Paved surface**	**Building**	**Vegetation**	**Non-vegetation**	**Water**	**Total**	**User's accuracy**
Actual class	Paved surface	1,890,847	127,810	279,060	5205	2369	2,305,291	82.02%
	Building	65,609	1,771,164	58,877	943	2245	1,898,838	93.28%
	Vegetation	169,500	217,278	5,281,476	21,308	431	5,689,993	92.82%
	Non-vegetation	7376	2896	11,885	72,959	0	95,116	76.71%
	Water	883	1311	177	1	8390	10,762	77.96%
	Total	2,134,215	2,120,459	5,631,475	100,416	13,435	10,000,000	
	Producer's accuracy	88.60%	83.53%	93.78%	72.66%	62.45%		**90.25%**

and complex roofs covered by vegetation (CV). The distinction between simple and complex roofs was that simple roofs had fewer than seven corners. Validation metrics included MAE, MAPE, and bias.

3 | RESULTS

3.1 | Image classification

The DL model was trained over 60 epochs on a computing setup that included an Intel Xeon Silver 4214R CPU at 2.40 GHz, 32 GB of RAM, and an NVIDIA RTX A4000 GPU. The training was completed in 10 h, whereas the testing phase was extended to 122 h. The model's output demonstrates its ability to accurately delineate urban features such as streets, sidewalks, buildings, and water bodies. Despite these strengths, the model exhibits limitations in identifying features obscured by tree canopies due to its reliance on pixel-based classification as shown in Figure 5b.

Validation of the model's performance yielded an overall accuracy of 90.25%, as documented in Table 1. Additionally, a kappa statistic of 0.85 indicates a high level of agreement between the model's predictions and the actual classifications. This statistic confirms the model's effectiveness, but it struggles with features hidden under tree cover.

Buildings and vegetation demonstrated the highest user's accuracy among the classes, with vegetation also achieving higher producer's accuracy than buildings. The relatively lower accuracy observed in vegetation and non-vegetation classes may decrease from the gradational nature of their boundaries. In contrast to the distinct shapes and boundaries of other classes, such as paved surfaces with distinct and clearly defined borders, the boundary between vegetative and non-vegetative areas (e.g., bare soils) is often present in the interlaced pattern. This posed a challenge in digitizing and labeling images for ground truth, leading to uncertainties in the classification results.

3.2 | Street improvement

The correction effort constructed the paved surface class beneath the tree canopy. As demonstrated in Figure 6a–c, the approach effectively connected the paved surface class under trees covering both sides of a street. In the original classification (Figure 6b), two pavement polygons were separated by tree canopies. After applying the proposed method, these pavement polygons were connected while maintaining the consistent width of the street (Figure 6c). This outcome would help construct a fully connected street network at the city scale.

Based on the validation results, the original classification substantially underestimated the pavement surface class across 50 randomly chosen streets. After the post-classification improvement, street features had been expanded to cover areas beneath canopies, resulting in a closer alignment with the ground truth. The efficacy of the post-classification improvements was underscored by the substantial reductions in MAE from 244.90 to 57.17 m^2 and in MAPE from 6.79% to 1.83% as detailed in Table 2. The R^2 value also improved to an ideal 1.00, indicating a perfect fit. The completeness of the street classification had improved markedly from 93.22% before the correction to 98.17% after the correction. Furthermore, the Wilcoxon signed-rank test yielded a p-value of less than .0001, signifying a statistically significant difference in the classification accuracy before and after the improvement.

3.3 | Sidewalk improvement

Sidewalk improvement was notably enhanced by the recovery of the paved surface class affected by tree canopy. Three examples are shown in Figure 6d–f. In the two examples of parallel sidewalks (Figure 6d–e), the method accurately captured the sidewalks on both sides of the street. In the example of the cul-de-sac sidewalk (Figure 6f), the correction was based on the circumcircle derived from

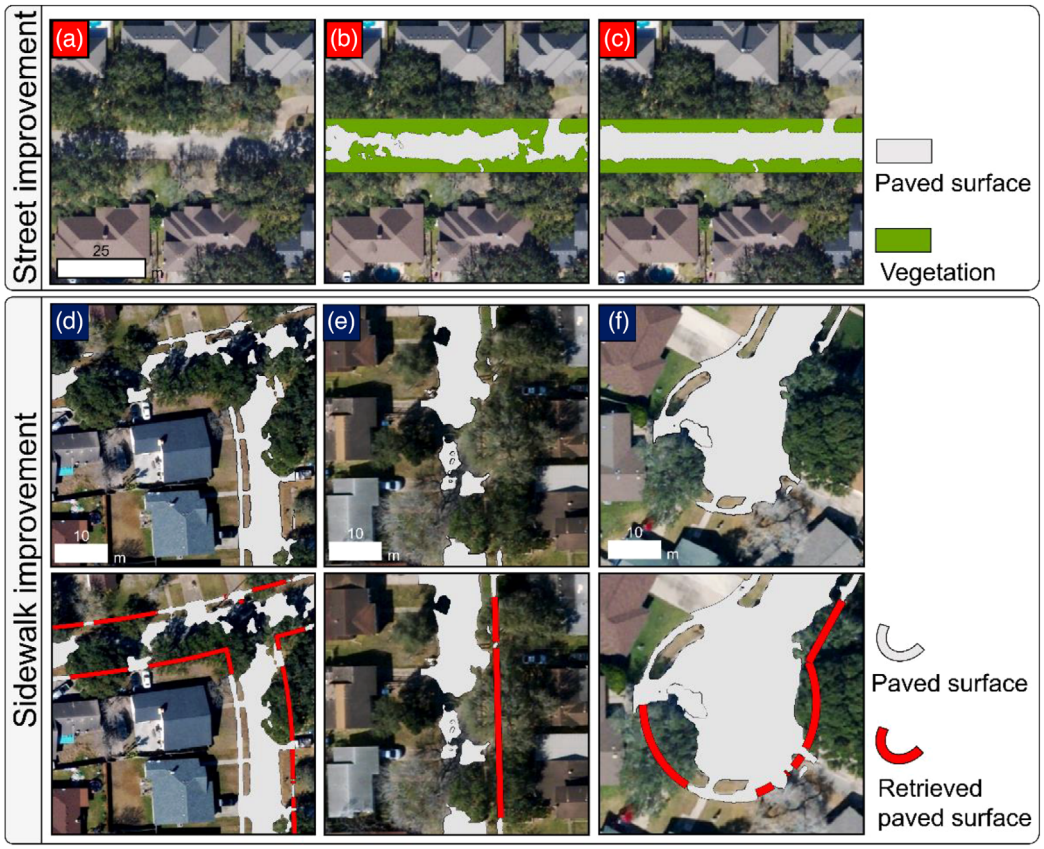

FIGURE 6 An example of street improvement: (a) the HxGN image of a street obscured by tree canopy; (b) discontinued street from the original classification; (c) continued street after the correction. Examples of sidewalk improvement; (d) parallel sidewalks on both sides; (e) parallel sidewalk on one side; (f) cul-de-sac sidewalk. Red lines highlight the retrieved pavement after the correction.

TABLE 2 Comparison of original and post-classification improvement metric values for street and sidewalk.

Feature	Comparison basis	Mean absolute error (MAE)		Mean absolute percentage error (MAPE)		R^2		Completeness		Wilcoxon *p*-value
		Before	After	Before	After	Before	After	Before	After	Before versus after
Street	Ground truth (area)	244.90 m^2	57.17 m^2	6.79%	1.83%	0.92	1.00	93.22%	98.17%	<.0001
Sidewalk	Ground truth (length)	60.59 m	41.15 m	14.14%	12.43%	0.87	0.94	56.86%	81.85%	<.0001

the medial axis of the sidewalk, and the merging process successfully filled the gap between the retrieved sidewalk segments (red lines) and the original classification result (gray polygons).

The validation of sidewalk improvements involved 100 randomly selected street segments, with an average segment length of 163.00 m. Among these, 57 segments were affected by canopy cover, resulting in 3463.53 m of sidewalks obscured by tree canopies. Initially, the MAE and MAPE values before the correction were 60.59 m and 14.14%, respectively, with a completeness of only 56.86%, as detailed in Table 2. After implementing the post-classification improvement, these metrics improved significantly. Post-classification processing improvement reduced the MAE to 41.15 m and the MAPE to 12.43%. Additionally, the R^2 value increased to 0.94, indicating a high level of model accuracy. The completeness of the sidewalk classification also improved dramatically, rising from 56.86% to 81.85%. This increase in completeness signifies a substantial enhancement in capturing the actual extent of sidewalks. The improved detection reflects a more accurate and usable representation of urban infrastructure for planning and navigation purposes. Furthermore, the Wilcoxon signed-rank test confirmed a statistically significant

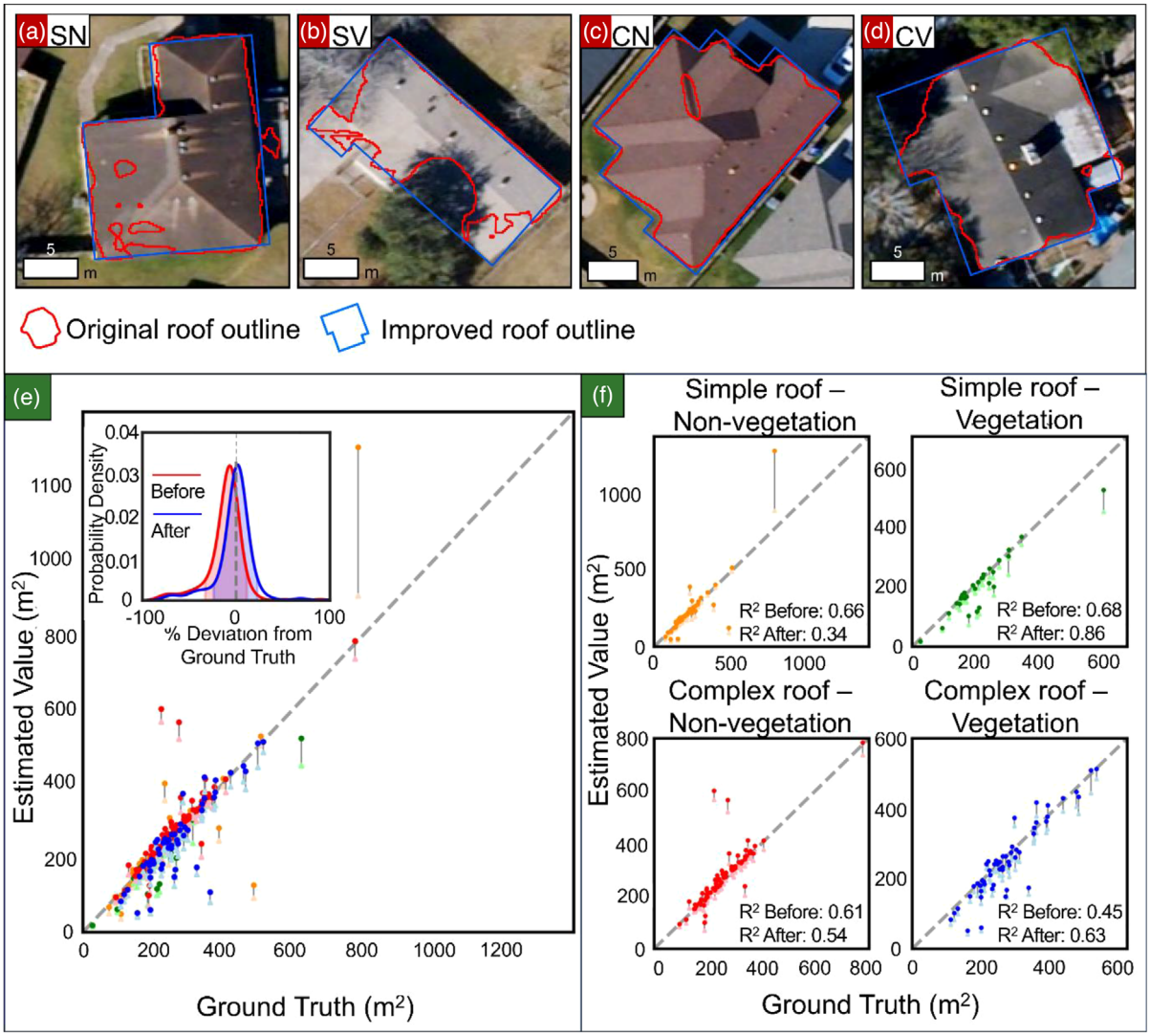

FIGURE 7 Examples of roof improvement: (a) simple roof—non-vegetation; (b) simple roof—vegetation; (c) complex roof—non-vegetation; (d) complex roof—vegetation. Validation of roof improvement: (e) estimated roof area across all roof types; (f) estimated roof area for each type. Light-color markers indicate the before correction, and dark-color markers indicate the after correction.

difference in the sidewalk classification accuracy before and after the improvement, with a *p*-value of less than .0001.

3.4 | Roof improvement

The application of roof improvement successfully increased the roof obscured by tree canopies for all four roof types (Figure 7a–d). The correction improved according to the validation based on 200 land parcels (Figure 7e,f and Table 3). This post-classification improvement method improved the MAE from 36.44 to 30.56, the MAPE from 15.30% to 12.17%, and most notably, the bias from −24.82 to 0.43, all indicating the improvement of initial underestimation. The overall improvement is also evident in terms of the probability density function of the roof areas (Figure 7e). The probability density function indicates a convergence of the mean deviation toward zero, reflecting a post-classification improvement alignment of roof area estimates with ground truth.

A closer analysis in Figure 7f and Table 3 revealed distinct outcomes for various roof types. The method excelled with SV and CV roofs affected by tree canopies, with bias significantly improving post-classification for SV roofs to −17.80, indicating that half of the missing areas were retrieved. The slight increases in MAE and MAPE for SN roofs were caused by the classification performance in just one parcel, where specific roof materials appeared to be less distinguishable from the shadow of large buildings. Excluding this outlier would lead to MAE and MAPE values lower than pre-correction levels as expected. Roofs not covered by tree canopies, particularly SN and CN, showed a slight oversimplification. The minor error increases for

TABLE 3 Additional performance metrics of roof improvement.

	MAE (m^2)		MAPE (%)		Bias (m^2)	
Roof type	**Before**	**After**	**Before**	**After**	**Before**	**After**
Overall	36.44	30.56	15.30	12.17	−24.82	0.43
SN	33.64	38.05	13.87	12.73	−21.88	6.90
SV	40.31	23.10	19.08	11.43	−40.31	−17.80
CN	27.08	27.75	11.50	11.64	−4.79	18.75
CV	48.17	31.55	19.17	12.71	−43.58	17.80

Abbreviations: CN, complex roofs not covered by vegetation; CV, complex roofs covered by vegetation; SN, simple roofs not covered by vegetation; SV, simple roofs covered by vegetation.

these roofs were due to their already well-defined outlines from the initial classification; post-correction adjustments primarily involved orthogonalizing these outlines, which did not yield significant improvements. Ultimately, the proposed method facilitated a systematic representation of roof geometries across the study area, reducing the irregularities of individual roof structures and contributing to a more uniform urban topology.

The validation results for the three features of streets, sidewalks, and roofs demonstrated successful recovery based on the reduced error metrics from the post-classification procedure. This confirms that retrieving features under tree canopies to increase impervious area is valid. Applying these post-classification improvement techniques increased the impervious area, including paved surfaces and building classes, by 4.98 km^2 from 104.15 to 109.13 km^2. This increase accounts for a 4.78% rise in impervious surface, compared to the original classification, and a 1.52% increase in the total impervious surface of the study area.

4 | DISCUSSION

4.1 | Benefits of very high-resolution imagery

This resolution enables the differentiation of crucial urban features, such as buildings, streets, sidewalks, and even sidewalk gardens. Distinguishing these features is essential for accurately identifying and quantifying impervious surfaces, a major component of the urban landscape that significantly influences the hydraulic and hydrological processes underlying various green and grey stormwater infrastructures. Furthermore, very high-resolution imagery facilitates the detection of built structures within land parcels, revealing variations in their sizes and distributions. This capability is crucial for accurately assessing surface imperviousness at the individual parcel level and has important implications for urban water management practices such as stormwater fee calculations (Lee et al., 2023). The recent availability of centimeter-level resolution aerial imagery, such as Hexagon's datasets, offers unprecedented detail for urban analysis. This work employs the well-established DeepLabV3+ DL model as a strong baseline for pixel classification (M. Liu et al., 2021; Tong et al., 2023). While newer models might offer slight accuracy improvements, this study focuses on demonstrating the effectiveness of accessible algorithms paired with high-resolution data. To further enhance our methodologies, adapting end-to-end deep learning models and exploring dynamic ensemble learning algorithms could improve the management of urban landscape complexity (Alam et al., 2020; Hassanpour et al., 2019). Similarly, incorporating self-supervised learning techniques might enhance feature extraction without the need for extensive labeled datasets (Rafiei et al., 2024). However, pixel classification accuracy remains limited by misrepresenting surface features under tree canopies, as the model can only classify what it sees and cannot detect the features masked by the canopies. Therefore, correcting the land cover data is essential to improve the accuracy and connectivity of ground features, highlighting the significance of post-classification processing. In contrast, lower-resolution land cover data generated from lower-resolution imagery cannot provide the detail necessary for accurate feature correction. Overall, land cover data derived from very high-resolution aerial imagery strike an optimal balance between detail and coverage, surpassing the capabilities of both UAS and satellite images.

4.2 | Comparative analysis of urban feature correction methods

To accurately delineate urban features obscured by tree canopies, our method leverages readily accessible street centerline and land parcel data. This approach offers several advantages over methodologies that rely on auxiliary surface datasets such as Google Street View (Ning, Li, et al., 2022; Ning, Ye, et al., 2022; Verma et al., 2021). While potentially valuable, Google Street View data can be

inconsistent due to varying acquisition dates (2011–2023) in the case study area. This inconsistency can compromise the accuracy of corrections, especially in rapidly changing urban landscapes. Furthermore, vehicles (both parked and moving) often obstruct street-level imagery, limiting its effectiveness in correcting features under canopies. The labor-intensive processing requirements of street-level panoramic imagery present significant challenges for city-scale projects that require substantial resources. To address the challenges of delineating features obscured by tree canopies, our method leverages readily accessible street centerline and land parcel data. This vector-based approach offers several advantages. First, it can ensure consistent data quality despite frequent updates of street centerline and land parcel data and reflect the ensuring alignment with the latest construction or landscape changes. Second, unlike street-level imagery, which can be obstructed by vehicles and affected by perspective issues, vector data can delineate urban features without such limitations. Finally, this method is integrated with the initial image classification, and the seamless workflow can reduce information loss, distortion, and uncertainty during data conversion and exchanges. This approach significantly reduces processing requirements, compared to street-level image methods, which involve redundant classification steps.

Airborne LiDAR datasets, while offering insights into urban topography, also present limitations. First, their availability is still restricted in many regions. Second, even when the LiDAR datasets are available, their temporal discrepancies with aerial imagery can pose challenges. For example, in the case study area, the latest LiDAR dataset dates to 2018 (United States Geological Survey, 2018). It cannot capture the changes in the residential expansion that are evident in the 2021 aerial imagery. This temporal mismatch highlights the challenges of relying on LiDAR for accurate feature correction in rapidly changing urban environments. Furthermore, the available LiDAR point cloud density of the study area (2.5 points/m^2) may be insufficient for delineating fine-scale features covered by tree canopies, especially compared to the high-resolution of our 15-cm land cover data. The recent study indicates that higher point cloud densities (4–123 points/m^2) are necessary for accurate roof modeling and feature correction, with the smallest detectable area being determined by point density (Hu et al., 2021). However, the availability and cost of acquiring high-density LiDAR data and the potential limitations of relying solely on outdated or obstructed street-view perspectives highlight the need for alternative approaches. Readily available vector data sources such as TIGER (US-specific) and OpenStreetMap (global) offer advantages for accurate feature extraction and ensure the broader applicability of this method (OpenStreetMap Contributors, 2023; United States Census Bureau, 2023). These readily available vector datasets provide a cost-effective and widely accessible solution for accurate land cover correction.

4.3 | Limitations and adapting our method to different geographical contexts

The proposed method can be improved in several ways. One of the most significant limitations of this method is the dependency on high-resolution and high-quality land cover data. The post-classification processing will be compromised if the resolution is coarser than typical urban features (such as sidewalks) or too imprecise to delineate actual building footprints. Therefore, ensuring an appropriate source of high-resolution land cover data is vital before applying this approach. Beyond land cover data, the method relies on the availability and quality of street centerline and land parcel vector data. Variations in the detail and accuracy of these datasets across different regions could necessitate adjustments to the approach. For example, if street centerline data lack a street width field, it might be necessary to omit post-classification street improvements. Additionally, our method currently relies on four assumptions about urban layout to predict or project features obscured by tree canopies, and each assumption presents specific limitations:

1. Sidewalk alignment (parallel to streets): The method assumes sidewalks that run directly parallel to streets, as it relies on a calculated distance value (mode) that remains constant for each street segment. Example: Curvilinear sidewalks that deviate significantly from the street segments will be inaccurately predicted due to inconsistent distances.
2. Sidewalk presence (entirely present or absent): The method assumes a sidewalk that either runs the entire length of a street segment between intersections or is absent, as it delineates sidewalks by creating a buffer along the whole street segment. Example: Sidewalks that only exist for a portion of a street segment (e.g., disappearing mid-block between intersections) will not be accurately corrected.
3. Sidewalk width (consistent and city code compliant): The method assumes sidewalks adhere to a predictable width based on city guidelines. Example: Areas with irregular sidewalk designs or violations of city codes will result in errors in the predicted sidewalk area.
4. Residential roof geometry (predominantly orthogonal): The method relies on the minimum bounding area, which works best with orthogonal roof shapes covering features partially obscured by tree canopies. Example:

Unique architectural designs with circular, triangular, or complex roof geometries might introduce inaccuracies during roof boundary extraction due to their shape deviating from the orthogonal assumption. Features completely covered by tree canopies may not be corrected.

Despite these limitations, the core principles of this method hold potential for broader application. Our study in Corpus Christi, TX, highlights the potential for broader application characteristics, including a grid-based street layout and a prevalence of detached housing with associated sidewalks. The reliance on readily accessible vector data and the streamlined correction process offers advantages over methods dependent on auxiliary surface datasets. Assessing how closely a city conforms to the urban layout assumptions is critical. In cases of significant deviation, algorithmic changes might be introduced. One example where algorithmic adaptation may be necessary is handling sidewalk segments obscured by tree cover. Instead of relying on a simple distance-based prediction, curvilinear regression models could be used to capture sidewalk trajectories better. This involves generating a regression model using the measurable distances between the street centerline and visible sidewalk portions to predict the obscured sections. Another area for adaptation is roof analysis. The proposed approach relies on identifying the minimum bounding box, which assumes a predominance of orthogonal roof edges. This method will be ineffective in locations with complex roof shapes or where a large portion of the roofs are entirely obscured by tree cover. In addition, open courtyards pose a challenge for the minimum bounding box concept. Their internal features (vegetation and pavement) can lead to misclassification, as our method may incorrectly identify them as part of the building footprint. This is common in European cities with frequent courtyard designs (Edwards et al., 2004). To address inaccuracies stemming from deviations in our assumptions, incorporating additional data sources or exploring adjustments to the algorithm could provide solutions. Crucially, it is essential to balance these algorithmic adaptations with computational costs. Complex methods can prove computationally expensive and potentially impractical for large-scale city analysis. It is best to assess the trade-offs carefully based on the specific characteristics and scale of the city under investigation.

5 | CONCLUSION

The research presented marks a significant advancement in urban land cover classification using 15-cm resolution 4-band aerial imagery. This approach comprehensively depicted Corpus Christi, TX, covering a 312 km^2 area and employed the DeepLabV3+ model with a ResNet-101 backbone. The training dataset, which accounted for 0.21% of the total study area, was labeled across five classes. The DL model achieved a total accuracy of 90.25%, revealing the potential of high-resolution imagery to capture intricate urban details at the parcel level. Such an advancement is particularly valuable for precise urban analysis and planning.

Moreover, the study addressed the challenge of tree canopy coverage in urban environments by integrating statistical and geometrical analysis with vector data to process the land cover dataset, focusing on accurately representing impervious surfaces covered by canopies. This post-classification correction significantly improved the depiction of urban features, including streets, sidewalks, and roofs. It showed an increase in the impervious surface area, accounting for 4.78% of the original impervious surface classification or 1.52% of the total study area. While these improvements may seem minimal, they are crucial for enhancing data functionality, ensuring continuity in impervious surfaces, preserving road areas under canopies, networking sidewalks, and refining roof geometries. Furthermore, this research converts raster data derived from a unimodal surface dataset into vector formats, streamlining the land cover analysis process. This approach improves urban landscape classification and ensures accurate delineation of impervious surfaces from a single surface dataset, enhancing data quality and reducing issues related to temporal mismatches, computation time, and resource use. This study establishes a new standard by advancing post-classification techniques with high-resolution aerial imagery, significantly enhancing the delineation and analysis of urban features. These improvements in detail and accuracy directly support more informed decision-making in urban infrastructure development and environmental planning.

ACKNOWLEDGMENTS

We thank the editor and five reviewers for their valuable insights and suggestions. This work was supported by the National Science Foundation (NSF) under Grants 2050986 and 2112631 and the National Aeronautics and Space Administration (NASA) under Grant 80NSSC22K1670 to Texas A&M University–Corpus Christi. Any opinions, findings, conclusions, or recommendations expressed in this material are those of the authors and do not necessarily reflect the views of NSF and NASA. We thank Icograms (icograms.com) for providing services and materials in developing Figure 5a.

ORCID

Lapone Techapinyawat https://orcid.org/0000-0001-5653-3971

REFERENCES

Alam, K. M. R., Siddique, N., & Adeli, H. (2020). A dynamic ensemble learning algorithm for neural networks. *Neural Computing and Applications*, *32*(12), 8675–8690. https://doi.org/10.1007/s00521-019-04359-7

Amani, M., Mahdavi, S., Kakooei, M., Ghorbanian, A., Brisco, B., DeLancey, E., Toure, S., & Reyes, E. L. (2021). Wetland change analysis in Alberta, Canada using four decades of Landsat imagery. *IEEE Journal of Selected Topics in Applied Earth Observations and Remote Sensing*, *14*, 10314–10335. https://doi.org/10.1109/JSTARS.2021.3110460

Bergsma, E. W. J., & Almar, R. (2020). Coastal coverage of ESA' Sentinel 2 mission. *Advances in Space Research*, *65*(11), 2636–2644. https://doi.org/10.1016/j.asr.2020.03.001

Bodansky, E., Gribov, A., & Pilouk, M. (2002). Smoothing and compression of lines obtained by raster-to-vector conversion. In D. Blostein & Y. B. Kwon (Eds.), *Graphics recognition algorithms and applications. GREC 2001. Lecture notes in computer science* (Vol. *2390*). Springer. https://doi.org/10.1007/3-540-45868-9_22

Braik, A. M., & Koliou, M. (2024). Automated building damage assessment and large-scale mapping by integrating satellite imagery, GIS, and deep learning. *Computer-Aided Civil and Infrastructure Engineering*. Advance online publication. https://doi.org/10.1111/MICE.13197

Edwards, B., Sibley, M., Hakmi, M., & Land, P. (Eds.). (2004). *Courtyard housing*. Taylor & Francis. https://doi.org/10.4324/9780203646724

Chen, L.-C., Zhu, Y., Papandreou, G., Schroff, F., & Adam, H. (2018). Encoder-decoder with atrous separable convolution for semantic image segmentation. In V. Ferrari, M. Hebert, C. Sminchisescu, & Y. Weiss (Eds.), *Computer vision—ECCV 2018. ECCV 2018. Lecture notes in computer science* (Vol. 11211, pp. 833–851). Springer. https://doi.org/10.1007/978-3-030-01234-2_49

City of Corpus Christi GIS Services. (2018). *City of Corpus Christi land use*. City of Corpus Christi.

City of Corpus Christi GIS Services. (2023). *City of Corpus Christi land parcel and street centerline*. City of Corpus Christi. https://gis-corpus.opendata.arcgis.com

Douglas, D. H., & Peucker, T. K. (2011). Algorithms for the reduction of the number of points required to represent a digitized line or its caricature. In M. Dodge (Ed.), *Classics in cartography* (pp. 15–28). John Wiley & Sons, Ltd. https://doi.org/10.1002/9780470669488.ch2

Du, S., Shi, P., Van Rompaey, A., & Wen, J. (2015). Quantifying the impact of impervious surface location on flood peak discharge in urban areas. *Natural Hazards*, *76*(3), 1457–1471. https://doi.org/10.1007/s11069-014-1463-2

Dunton, A., & Gardoni, P. (2023). Generating network representations of small-scale infrastructure using generally available data. *Computer-Aided Civil and Infrastructure Engineering*, *39*(8), 1143–1158. https://doi.org/10.1111/MICE.13137

Fu, B., Liu, M., He, H., Lan, F., He, X., Liu, L., Huang, L., Fan, D., Zhao, M., & Jia, Z. (2021). Comparison of optimized object-based RF-DT algorithm and SegNet algorithm for classifying Karst wetland vegetation communities using ultra-high spatial resolution UAV data. *International Journal of Applied Earth Observation and Geoinformation*, *104*, 102553. https://doi.org/10.1016/j.jag.2021.102553

Goetz, S. J., Wright, R. K., Smith, A. J., Zinecker, E., & Schaub, E. (2003). IKONOS imagery for resource management: Tree cover, impervious surfaces, and riparian buffer analyses in the mid-Atlantic region. *Remote Sensing of Environment*, *88*(1-2), 195–208. https://doi.org/10.1016/j.rse.2003.07.010

Hassanpour, A., Moradikia, M., Adeli, H., Khayami, S. R., & Shamsinejadbabaki, P. (2019). A novel end-to-end deep learning scheme for classifying multi-class motor imagery electroencephalography signals. *Expert Systems*, *36*(6), e12494. https://doi.org/10.1111/exsy.12494

He, D., Shi, Q., Liu, X., Zhong, Y., Xia, G., & Zhang, L. (2022). Generating annual high resolution land cover products for 28 metropolises in China based on a deep super-resolution mapping network using Landsat imagery. *GIScience & Remote Sensing*, *59*(1), 2036–2067. https://doi.org/10.1080/15481603.2022.2142727

He, K., Zhang, X., Ren, S., & Sun, J. (2016). Deep Residual learning for image recognition. *2016 IEEE Conference on Computer Vision and Pattern Recognition (CVPR)*, Las Vegas, NV (pp. 770–778). https://doi.org/10.1109/CVPR.2016.90

Hexagon. (2021). *Hexagon aerial imagery*. Hexagon. https://hexagon.com/products/aerial-imagery

Hou, Q., & Ai, C. (2020). A network-level sidewalk inventory method using mobile LiDAR and deep learning. *Transportation Research Part C: Emerging Technologies*, *119*, 102772. https://doi.org/10.1016/j.trc.2020.102772

Hu, P., Miao, Y., & Hou, M. (2021). Reconstruction of complex roof semantic structures from 3D point clouds using local convexity and consistency. *Remote Sensing*, *13*(10), 1946. https://doi.org/10.3390/rs13101946

Kaur, N., Lee, C. C., Mostafavi, A., & Mahdavi-Amiri, A. (2023). Large-scale building damage assessment using a novel hierarchical transformer architecture on satellite images. *Computer-Aided Civil and Infrastructure Engineering*, *38*(15), 2072–2091. https://doi.org/10.1111/MICE.12981

Khanwilkar, S., Galletti, C., Mondal, P., Urpelainen, J., Nagendra, H., Jhala, Y., Qureshi, Q., & DeFries, R. (2023). Land cover and forest health indicator datasets for central India using very-high resolution satellite data. *Scientific Data*, *10*(1), 738. https://doi.org/10.1038/s41597-023-02634-w

Kimpton, T., Higuera, P., Whittaker, C., Wotherspoon, L., & Zorn, C. (2024). A rapid simplified method for determining tsunami inundation extent based on energy conservation. *Computer-Aided Civil and Infrastructure Engineering*. Advance online publication. https://doi.org/10.1111/MICE.13168

Krapf, S., Willenborg, B., Knoll, K., Bruhse, M., & Kolbe, T. H. (2022). Deep learning for semantic 3D city model extension: Modeling roof superstructures using aerial images for solar potential analysis. *ISPRS Annals of the Photogrammetry, Remote Sensing and Spatial Information Sciences, X-4/W2-2022*, Sydney, Australia (pp. 161–168). https://doi.org/10.5194/isprs-annals-X-4-W2-2022-161-2022

Lee, J., Zhang, H., & Huang, Y. (2023). Toward a more socially equitable stormwater management fee: The case of Corpus Christi in Texas, USA. *Environment and Planning B: Urban Analytics and City Science*, *51*(4), 939–953. https://doi.org/10.1177/23998083231207535

Li, J., & Bortolot, Z. J. (2022). Quantifying the impacts of land cover change on catchment-scale urban flooding by classifying aerial

images. *Journal of Cleaner Production*, *344*, 130992. https://doi.org/10.1016/j.jclepro.2022.130992

Li, L., Song, N., Sun, F., Liu, X., Wang, R., Yao, J., & Cao, S. (2022). Point2Roof: End-to-end 3D building roof modeling from airborne LiDAR point clouds. *ISPRS Journal of Photogrammetry and Remote Sensing*, *193*, 17–28. https://doi.org/10.1016/j.isprsjprs.2022.08.027

Li, Q., Krapf, S., Shi, Y., & Zhu, X. X. (2023). SolarNet: A convolutional neural network-based framework for rooftop solar potential estimation from aerial imagery. *International Journal of Applied Earth Observation and Geoinformation*, *116*, 103098. https://doi.org/10.1016/j.jag.2022.103098

Li, X., Li, Z., Feng, R., Luo, S., Zhang, C., Jiang, M., & Shen, H. (2019). Generating high-quality and high-resolution seamless satellite imagery for large-scale urban regions. *Remote Sensing*, *12*(1), 81. https://doi.org/10.3390/rs12010081

Liu, M., Fu, B., Fan, D., Zuo, P., Xie, S., He, H., Liu, L., Huang, L., Gao, E., & Zhao, M. (2021). Study on transfer learning ability for classifying marsh vegetation with multi-sensor images using DeepLabV3+ and HRNet deep learning algorithms. *International Journal of Applied Earth Observations and Geoinformation*, *103*, 102531. https://doi.org/10.1016/j.jag.2021.102531

Liu, Y., Zhang, B., Wang, L., & Wang, N. (2013). A self-trained semisupervised SVM approach to the remote sensing land cover classification. *Computers & Geosciences*, *59*, 98–107. https://doi.org/10.1016/j.cageo.2013.03.024

MMSegmentation Contributors. (2020). *OpenMMLab semantic segmentation toolbox and benchmark*. https://Github.Com/Open-Mmlab/Mmsegmentation

National Centers for Environmental Information (NCEI). (2023). *Global summary of the year 2013 - 2023*. https://www.Ncei.Noaa.Gov/

Ning, H., Li, Z., Wang, C., Hodgson, M. E., Huang, X., & Li, X. (2022). Converting street view images to land cover maps for metric mapping: A case study on sidewalk network extraction for the wheelchair users. *Computers, Environment and Urban Systems*, *95*, 101808. https://doi.org/10.1016/j.compenvurbsys.2022.101808

Ning, H., Ye, X., Chen, Z., Liu, T., & Cao, T. (2022). Sidewalk extraction using aerial and street view images. *Environment and Planning B: Urban Analytics and City Science*, *49*(1), 7–22. https://doi.org/10.1177/2399808321995817

Nofal, O., Rosenheim, N., Kameshwar, S., Patil, J., Zhou, X., van de Lindt, J. W., Duenas-Osorio, L., Cha, E. J., Endrami, A., Sutley, E., Cutler, H., Lu, T., Wang, C., & Jeon, H. (2024). Community-level post-hazard functionality methodology for buildings exposed to floods. *Computer-Aided Civil and Infrastructure Engineering*, *39*(8), 1099–1122. https://doi.org/10.1111/MICE.13135

Ogden, F. L., Raj Pradhan, N., Downer, C. W., & Zahner, J. A. (2011). Relative importance of impervious area, drainage density, width function, and subsurface storm drainage on flood runoff from an urbanized catchment. *Water Resources Research*, *47*(12). https://doi.org/10.1029/2011WR010550

OpenStreetMap contributors. (2023). *Street Shapefile*. https://www.openstreetmap.org/

Order of the City Council. (2004). *Chapter 49—Streets and sidewalks, general ordinances of the city*. https://library.municode.com/tx/corpus_christi/codes/code_of_ordinances

Poole, J. M., Carr, W. R., Price, D. M., & Singhurst, J. R. (2005). *Rare plants of Texas*. Texas A & M University Press.

Qin, J., Shangguan, Z., & Xi, W. (2019). Seasonal variations of leaf traits and drought adaptation strategies of four common woody species in South Texas, USA. *Journal of Forestry Research*, *30*(5), 1715–1725. https://doi.org/10.1007/s11676-018-0742-2

Rafiei, M. H., Gauthier, L. V., Adeli, H., & Takabi, D. (2024). Self-supervised learning for electroencephalography. *IEEE Transactions on Neural Networks and Learning Systems*, *35*(2), 1457–1471. https://doi.org/10.1109/TNNLS.2022.3190448

Rana, V. K., & Venkata Suryanarayana, T. M. (2020). Performance evaluation of MLE, RF and SVM classification algorithms for watershed scale land use/land cover mapping using sentinel 2 bands. *Remote Sensing Applications: Society and Environment*, *19*, 100351. https://doi.org/10.1016/j.rsase.2020.100351

Roy, D. P., Wulder, M. A., Loveland, T. R., Woodcock, C. E., Allen, R. G., Anderson, M. C., Helder, D., Irons, J. R., Johnson, D. M., Kennedy, R., Scambos, T. A., Schaaf, C. B., Schott, J. R., Sheng, Y., Vermote, E. F., Belward, A. S., Bindschadler, R., Cohen, W. B., Gao, F., … Zhu, Z. (2014). Landsat-8: Science and product vision for terrestrial global change research. *Remote Sensing of Environment*, *145*, 154–172. https://doi.org/10.1016/j.rse.2014.02.001

Scepanovic, S., Antropov, O., Laurila, P., Rauste, Y., Ignatenko, V., & Praks, J. (2021). Wide-area land cover mapping with sentinel-1 imagery using deep learning semantic segmentation models. *IEEE Journal of Selected Topics in Applied Earth Observations and Remote Sensing*, *14*, 10357–10374. https://doi.org/10.1109/JSTARS.2021.3116094

Shevyrev, S., & Carranza, E. J. M. (2022). Application of maximum entropy for mineral prospectivity mapping in heavily vegetated areas of Greater Kurile Chain with Landsat 8 data. *Ore Geology Reviews*, *142*, 104758. https://doi.org/10.1016/j.oregeorev.2022.104758

Shuster, W. D., Bonta, J., Thurston, H., Warnemuende, E., & Smith, D. R. (2005). Impacts of impervious surface on watershed hydrology: A review. *Urban Water Journal*, *2*(4), 263–275. https://doi.org/10.1080/15730620500386529

Sohn, W., Kim, J. H., Li, M. H., Brown, R. D., & Jaber, F. H. (2020). How does increasing impervious surfaces affect urban flooding in response to climate variability? *Ecological Indicators*, *118*, 106774. https://doi.org/10.1016/J.ECOLIND.2020.106774

Tong, X. Y., Xia, G. S., & Zhu, X. X. (2023). Enabling country-scale land cover mapping with meter-resolution satellite imagery. *ISPRS Journal of Photogrammetry and Remote Sensing*, *196*, 178–196. https://doi.org/10.1016/J.ISPRSJPRS.2022.12.011

United States Census Bureau. (2023). *TIGER/Line Shapefiles*. https://www.census.gov/

United States Geological Survey. (2018). *2018 South Texas {LiDAR} data*. https://www.usgs.gov/products/maps/gis-data

Verma, D., Mumm, O., & Carlow, V. M. (2021). Identifying streetscape features using VHR imagery and deep learning applications. *Remote Sensing*, *13*(17), 3363. https://doi.org/10.3390/rs13173363

Wang, Y., Gao, L., Hong, D., Sha, J., Liu, L., Zhang, B., Rong, X., & Zhang, Y. (2021). Mask DeepLab: End-to-end image segmentation for change detection in high-resolution remote sensing images. *International Journal of Applied Earth Observation and Geoinformation*, *104*, 102582. https://doi.org/10.1016/j.jag.2021.102582

Wilcoxon, F. (1992). *Individual comparisons by ranking methods*. 196–202. https://doi.org/10.1007/978-1-4612-4380-9_16

Wulder, M. A., Roy, D. P., Radeloff, V. C., Loveland, T. R., Anderson, M. C., Johnson, D. M., Healey, S., Zhu, Z., Scambos, T. A., Pahlevan, N., Hansen, M., Gorelick, N., Crawford, C. J., Masek, J. G., Hermosilla, T., White, J. C., Belward, A. S., Schaaf, C., Woodcock, C. E., … Cook, B. D. (2022). Fifty years of Landsat science and impacts. *Remote Sensing of Environment*, *280*, 113195. https://doi.org/10.1016/j.rse.2022.113195

Yoo, S., Lee, J., Gholami Farkoushi, M., Lee, E., & Sohn, H.-G. (2022). Automatic generation of land use maps using aerial orthoimages and building floor data with a Conv-Depth Block (CDB) ResU-Net architecture. *International Journal of Applied Earth Observation and Geoinformation*, *107*, 102678. https://doi.org/10.1016/j.jag.2022.102678

Zhang, C., & Li, X. (2022). Land use and land cover mapping in the era of big data. *Land*, *11*(10), 1692. https://doi.org/10.3390/land11101692

Zhang, T., Su, J., Xu, Z., Luo, Y., & Li, J. (2021). Sentinel-2 satellite imagery for urban land cover classification by optimized random forest classifier. *Applied Sciences*, *11*(2), 543. https://doi.org/10.3390/app11020543

Zhang, W., Li, Z., & Shan, J. (2021). Optimal model fitting for building reconstruction from point clouds. *IEEE Journal of Selected Topics in Applied Earth Observations and Remote Sensing*, *14*, 9636–9650. https://doi.org/10.1109/JSTARS.2021.3110429

Zhu, Q., Guo, X., Deng, W., Shi, S., Guan, Q., Zhong, Y., Zhang, L., & Li, D. (2022). Land-Use/Land-Cover change detection based on a Siamese global learning framework for high spatial resolution remote sensing imagery. *ISPRS Journal of Photogrammetry and Remote Sensing*, *184*, 63–78. https://doi.org/10.1016/j.isprsjprs.2021.12.005

How to cite this article: Techapinyawat, L., Timms, A., Lee, J., Huang, Y., & Zhang, H. (2024). Integrated urban land cover analysis using deep learning and post-classification correction. *Computer-Aided Civil and Infrastructure Engineering*, 1–20. https://doi.org/10.1111/mice.13277